

# Joint processing of Landsat and ALOS-PALSAR data for forest mapping and monitoring

Eric A. Lehmann, *Member, IEEE*, Peter A. Caccetta, Zheng-Shu Zhou, *Member, IEEE*,  
Stephen J. McNeill, Xiaoliang Wu, and Anthea L. Mitchell

**Abstract**—Recent technological advances in the field of radar remote sensing have allowed the deployment of an increasing number of new satellite sensors. These provide an important source of Earth observation data which adds to the currently existing optical datasets. In parallel, the development of robust methods for global forest monitoring and mapping is becoming increasingly important. As a consequence, there is significant interest in the development of global monitoring systems that are able to take advantage of the potential synergies and complementary nature of optical and radar data. This paper proposes an approach for the combined processing of Landsat and ALOS-PALSAR data for the purpose of forest mapping and monitoring. This is achieved by incorporating the PALSAR data into an existing, operational Landsat-based processing system. Using a directed discriminant technique, a probability map of forest presence/absence is first generated from the PALSAR imagery. This SAR classification data is then combined with a time-series of similar Landsat-based maps within a Bayesian multi-temporal processing framework, leading to the production of a time series of joint radar–optical maps of forest extents. This approach is applied and evaluated over a pilot study area in north-eastern Tasmania, Australia. Experimental outcomes of the proposed joint processing framework are provided, demonstrating its potential for the integration of different types of remote sensing data for forest monitoring purposes.

**Index Terms**—Forest mapping and monitoring, remote sensing, ALOS-PALSAR, Landsat TM, multi-temporal processing, data fusion, discriminant analysis, conditional probability network.

## I. INTRODUCTION

THE recent launch of several international initiatives demonstrates the increasing need for global forest monitoring systems that provide estimates of carbon fluxes for the purpose of carbon accounting. Examples include the United Nations' REDD program (Reducing Emissions from Deforestation and Forest Degradation, [www.un-redd.org](http://www.un-redd.org))

initiated in 2008, and the Global Earth Observation System of Systems (GEOSS) developed since 2005 by the Group on Earth Observations (GEO, [www.earthobservations.org](http://www.earthobservations.org)). The GEO task on Forest Carbon Tracking (GEO-FCT, [www.geo-fct.org](http://www.geo-fct.org)), set up in 2008, aims to demonstrate that coordinated Earth observations can provide the basis for reliable forest information services of suitable consistency and accuracy to support the operation of global forest carbon estimation and reporting systems under the United Nations' Framework Convention on Climate Change (UNFCCC, [www.unfccc.int](http://www.unfccc.int)). In response to the GEO-FCT task, the Australian Department of Climate Change and Energy Efficiency (DCCEE) has recently launched the International Forest Carbon Initiative (IFCI, [www.climatechange.gov.au](http://www.climatechange.gov.au)) which aims to increase international forest carbon monitoring and accounting capacity in accordance with emerging international reporting and verification requirements.

Optical-based land cover monitoring products have been available for many years in several parts of the world. Examples include the CORINE land database supplied by the European Environmental Agency ([www.eea.europa.eu](http://www.eea.europa.eu)), the National Land Cover Database in the USA ([www.mrlc.gov](http://www.mrlc.gov)), and the Global Observation of Forest and Land Cover Dynamics program (GOFD-GOLD, [www.fao.org/gtos/gofc-gold](http://www.fao.org/gtos/gofc-gold)). In Australia, the Commonwealth Scientific and Industrial Research Organisation (CSIRO) has contributed to the development of the National Carbon Accounting System – Land Cover Change Program (NCAS-LCCP) [1], [2], in collaboration with the DCCEE and other partners. One component of this system offers the capability for fine-scale continental mapping and monitoring of the extent and change in perennial vegetation using Landsat satellite imagery, allowing for an effective estimation of greenhouse gas emissions from land use and land use changes [3]. This program currently uses over 7000 Landsat MSS/TM/ETM+ scenes resampled to a spatial resolution of 25m for nineteen time epochs since 1972 over continental Australia; it is now updated annually, making it one of the largest operational land cover monitoring programs of its kind in the world.

An important aspect in future developments of the NCAS framework under the International Forest Carbon Initiative involves taking advantage of new technologies in the area of space borne Synthetic Aperture Radar (SAR) sensors. While

Manuscript received September 24, 2010; revised June 17, 2011 and August 08, 2011; accepted September 11, 2011.

E. A. Lehmann is with the Commonwealth Scientific and Industrial Research Organisation (CSIRO), Division of Mathematics, Informatics and Statistics, 65 Brockway Road, Floreat WA 6014, Australia (phone: +61 (0)8 9333 6123, fax: +61 (0)8 9333 6121).

P. A. Caccetta, Z.-S. Zhou, and X. Wu are also with the CSIRO Division of Mathematics, Informatics and Statistics in Floreat, Western Australia.

S. J. McNeill, is with Landcare Research, Lincoln, New Zealand.

A. L. Mitchell is with the Cooperative Research Centre for Spatial Information (CRC-SI), School of Biological, Earth and Environment Sciences, the University of New South Wales, Sydney, Australia.

the availability of cloud-free Landsat images does not normally represent an issue for most of Australia, access to suitable optical datasets cannot always be guaranteed in all geographical areas [4], and especially those located in tropical regions or more southern latitudes such as Tasmania. For instance, the extent of cloud-affected areas over Tasmania in the nineteen Landsat mosaics of the NCAS archive is about 26% on average, ranging from 4% for the best year to 100% for the worst.<sup>1</sup> Missing optical data due to cloud cover is therefore a factor of particular importance in the development of global land cover monitoring systems, which need to operate under a variety of environmental and atmospheric conditions. In cloud-affected regions, the use of SAR data thus represents a valuable alternative to extend the current monitoring capabilities of existing optical systems [5]. A further benefit is the increased temporal coverage resulting from additional and/or complementary observations provided by SAR sensors. An improved accuracy in land cover mapping can also be expected when the complementary information from SAR data is considered jointly with existing optical datasets [6], [7]. Key aspects such as satellite data interoperability (obtaining the same thematic results with different sensors) and complementarity (adding thematic value by using two or more sensors) are therefore of specific interest in the development of joint radar–optical processing systems.

In the current literature, many studies can be found on the use of SAR data for forest mapping and monitoring. In particular, several papers investigate different approaches for the extraction of forest mapping information from JERS-1 and ERS-1/ERS-2 data in tropical regions, mainly for the purpose of detecting deforestation events [8], [9]. Examples of SAR-based methods for land cover discrimination include the use of decision tree classifiers [10], spectral mixing modeling techniques [11], support vector machine [12], [13], and hybrid learning classifiers [14]. Other existing works also consider the use of different SAR datasets such as RADARSAT [15], ALOS-PALSAR [16], and SIR-C/X-SAR [17]. In [18], an empirical investigation using multi-frequency SAR imagery (C-, L- and P-band) acquired from airborne platforms highlights the usefulness of longer-wavelength SAR data for forest monitoring and biomass estimation, thus paving the way towards monitoring systems using satellite data. Driven by the emergence of these new SAR technologies, further studies have also been recently carried out to investigate the synergetic potential of SAR and optical data; such comparative studies can be found, e.g., in [5] and [19]. Several articles also propose various methods for a combined processing (data fusion) of SAR and optical datasets for forest mapping and land cover classification, as described for instance in [20], [13], [6] and [7] (and references therein).

The use of data-level fusion techniques is based on the assumption that the different datasets under consideration are coincident in time. In the frame of the present research, a

series of comparative studies have also been carried out on the forest discrimination capabilities of combined SAR and optical data under the assumption of temporal coincidence. These studies are based on linear discriminant analysis and maximum likelihood classification for the same type of data as used in the present work (ALOS-PALSAR and Landsat TM), and the results are reported in [21]. The main outcomes indicate that: 1) considering the SAR and optical sensors jointly provides a better forest classification than either used independently, and 2) the respective contribution of each of the optical and SAR bands to the separation of different types of forest and non-forest land covers varies significantly. Readers are referred to [21] for more information on the specific forest discrimination properties of the data used in the present work (under the assumption of temporally coincident datasets).

The concepts described in this paper focus on a case where the assumption of coincident SAR and optical data cannot be made, due to constraints related to cloud cover and data source availability, for instance. This work thus investigates the interoperability of the SAR and optical sensors, where one sensor might be used to generate the information normally provided by the other. Current and future environmental monitoring systems will have the ability to draw on the (spatial and temporal) information provided by many satellite sensors operating at different wavelengths and with different acquisition times, and this paper presents a methodology for the integration of such multi-temporal data into a consistent probabilistic framework. One advantage of the proposed approach is that it independently combines the thematic information derived from the SAR and optical data at different times. This allows the interoperable use of one dataset when no information is available from the other, as in the case of cloud-affected Landsat imagery for instance. Two or more data streams (time-series) from different sensors can thus be efficiently integrated over time for improved forest monitoring capabilities (compared to the use of a single stream).

In support of the GEO-FCT task of forest mapping and monitoring, the proposed methodology is demonstrated here by considering a time series of ALOS-PALSAR and Landsat images over a test site in Tasmania. These data, together with an independent reference dataset, are described in Section II. Joint SAR–optical processing is achieved by first converting the SAR and Landsat data into maps of forest probabilities. A directed discriminant technique (canonical variate analysis, CVA) is used for this purpose, as explained in Section III. The resulting maps of forest probabilities are then processed jointly within the Bayesian framework of a conditional probability network (CPN), which is described in Section IV. Finally, Section V concludes this paper with a discussion of the main results presented in this work.

## II. DATA AND STUDY AREA

### A. Pilot study area

This work represents a pilot study carried out for a 66km × 50km demonstration area in the Ben Lomond region in north-

<sup>1</sup>NCAS aims to select the best available (most cloud-free) Landsat imagery in each epoch for forest mapping/monitoring across the Australian continent.

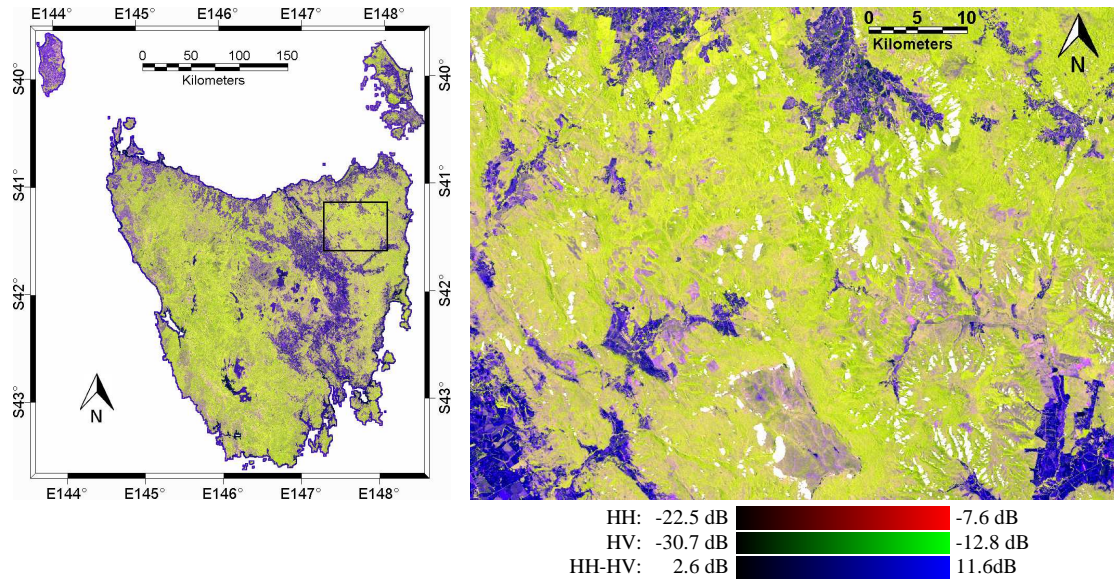


Fig. 1. ALOS-PALSAR dataset for 2008, HH/HV/HH-HV in R/G/B ( $\sigma^0$  in dB). *Left*: mosaic over Tasmania, with a box showing the 66km  $\times$  50km study area. *Right*: PALSAR data for the area of interest (centered on the latitude/longitude coordinates 41°24'33.1"S/147°40'12.1"E); white pixels correspond to the shadow mask. The color bars show the scales for the right-hand image.

eastern Tasmania, Australia (see Fig. 1, left). The centre of this study site is located at the latitude coordinate 41°24'33.1"S and longitude coordinate 147°40'12.1"E. This area includes one of Australia's national calibration sites (Mathinna region) defined in the framework of the GEO-FCT initiative. It contains a variety of land covers including rainforests, wet and dry eucalypt forests, exotic plantations for silviculture, agricultural land, as well as other cleared land (deforestation) and urban areas. Significant topographic variations can be found across the study site, with the terrain elevation varying between 85m and 1510m above sea level.

### B. ALOS-PALSAR data

The ALOS-PALSAR data used in this work was acquired at L-band ( $\sim$ 23.6cm wavelength) in fine-beam dual-polarization mode (HH and HV), in an ascending orbit and with the default off-nadir angle of 34.3°. The SAR data in the study area consists of a (cropped) mosaic of two PALSAR scenes, namely the scenes with path/row 381/6340 in the west (acquired on October 04, 2008) and path/row 380/6340 in the east (acquired on September 19, 2008). The single-look complex data (SLC level 1.1) was pre-processed according to the following steps:<sup>2</sup>

1. 8 $\times$ 2 multilooking (looks in range and azimuth, respectively) resulting in a pixel size of 29.8m  $\times$  25.1m
2. speckle filtering by means of adaptive 5 $\times$ 5 Lee filter [22]
3. radiometric calibration [23], [24], using a digital elevation model (DEM) with a 25m cell resolution, and radiometric normalization (modified cosine model) [25]
4. geocoding to 25m pixel size (to match the spatial resolution of Landsat) using the 25m DEM, and

<sup>2</sup>Steps 1, 2, 3, 4 and 6 in this processing sequence were carried out by means of the SAR processing software SARscape version 4.2.0 (<http://www.sarmap.ch/page.php?page=sarscape>).

calculation of the shadow areas<sup>3</sup>

5. terrain illumination correction [27], using the 25m DEM
6. creation of a two-scene mosaic (gradient mosaicking)
7. masking of the data using the shadow mask.

This processing sequence generates a mosaic of ortho-rectified, terrain-corrected and radiometrically calibrated PALSAR scenes at a resolution of 25m (Fig. 1, right), with values ranging from -22.5dB to -7.6dB in the HH channel, and from -30.7dB to -12.8dB in the HV channel (99% clip, i.e., excluding the first and last 0.5% of the data). The terrain illumination correction in Step 5 is necessary to compensate for illumination differences due to the local variations in topography and the viewing geometry of the SAR sensor. In areas of steep terrain, these factors typically lead to forward-facing slopes (facing toward the SAR sensor) appearing brighter and backward-facing slopes (facing away from the sensor) appearing darker. These effects limit the ability to extract relevant thematic information from the data and must therefore be corrected. Application of the terrain correction algorithm [27] to the SAR data was necessary as the SARscape product generated following Steps 3 and 4 still contained significant terrain-related artifacts (despite the correction for scattering area carried out as part of the radiometric calibration in Step 3, see [24]).

### C. Landsat TM data and derived products

#### 1) Data

The optical data used in this work was obtained from the existing archive of calibrated Landsat MSS/TM/ETM+ images produced as part of the NCAS-LCCP system. Within this

<sup>3</sup>In the study area, regions of SAR layover account for less than 0.01% of the pixels, and are therefore not treated separately in this work; in an operational setting, further processing of layover pixels can be implemented as described, for instance, in [26].

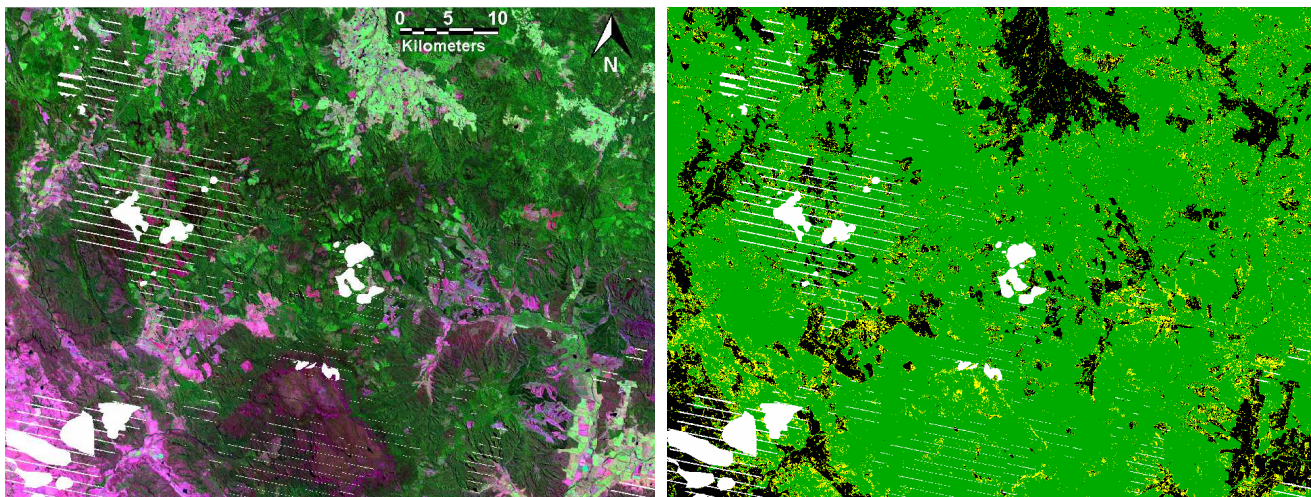


Fig. 2. Overview of Landsat data and forest/non-forest product. *Left*: 2008 Landsat TM dataset for the considered study area (bands 5/4/2 in R/G/B). Ben Lomond is the prominent rocky feature located in the centre-south of the image. *Right*: corresponding single-date forest probability map from the NCAS program for 2008, with forest probabilities of 100% shown in green, 0% in black, and values in between in yellow. In both images, white areas indicate regions masked out due to missing data (clouds and sensor deficiencies).

processing framework, all images need to be properly coregistered and calibrated in order to achieve meaningful land cover change information and to minimize errors related to misregistration. All Landsat scenes are processed according to strict quality standards [28] using the following steps:

1. orthorectification to a common spatial reference, using a rigorous earth-orbital model and a cross-correlation feature matching technique [2]
2. top-of-atmosphere reflectance calibration (sun angle and distance correction) [29]
3. correction of scene-to-scene differences using bi-directional reflectance distribution functions [30]
4. calibration to a common spectral reference using invariant targets [31]
5. correction for differential terrain illumination [32]
6. removal of corrupted data such as regions affected by smoke, clouds and sensor deficiencies
7. mosaicking of the individual Landsat scenes into 1:1,000,000 map sheets.

Key aspects of these processing steps are discussed in [28], [2], while full operational details are given in [33]. This process was used to generate a calibrated and orthorectified time series of Landsat mosaics over the Australian continent for a total of nineteen time slices between 1972 and 2010. For 2008, the optical data over the considered study area is a mosaic of two Landsat scenes acquired on January 14 and February 24, respectively (Fig. 2, left).

## 2) Forest probability maps

The main task initially undertaken as part of the NCAS program was the mapping of forest presence/absence (forest/non-forest, F/NF) from the Landsat time series. Continental maps of the forest extents across Australia were generated using a process involving the following steps:

1. identification of stratification zones, within which land cover types have similar spectral properties and are thus considered homogenous

2. creation of a base forest cover probability image by:
  - a. specification of a “single-date” classifier for each stratification zone, using ground and satellite data
  - b. identification of (soft) thresholds to determine the decision boundaries between F/NF classes, leading to a probability of forest cover for each pixel
3. creation of forest cover probability images for other epochs by means of a matching process [2], using the base probability image as reference
4. refinement of the single-date probability images using a spatial-temporal model for classification (Bayesian conditional probability network [34], [35]).

In Step 2, the single-date classifier is based on a directed discriminant technique called canonical variate analysis (CVA) [36]. This method determines the linear combination of image bands providing the best separation between the F/NF classes by maximizing the ratio of between-class to within-class variance (more details are provided in Section III.A). The image on the right in Fig. 2 shows the NCAS-LCCP forest probability image derived from the Landsat data for the area of interest in 2008. The subsequent use of a multi-temporal conditional probability network (CPN) in Step 4 improves the forest mapping accuracy and temporal consistency [1]. A comparison of alternative single-date classifiers was considered in [37] and demonstrates that the resulting differences in the forest presence/absence classifications are negligible after processing the single-date results with a CPN. As will be shown in Section IV, the CPN framework can also be used for the purpose of combining SAR and optical datasets into a single and consistent framework for forest mapping.

The present work considers the integration of the PALSAR dataset within this operational Landsat-based methodology (NCAS-LCCP). Some issues can be expected to arise when substituting data from a different sensor into this existing (legacy) framework. In particular, the results will be influenced by the specific biases introduced by each sensor, as

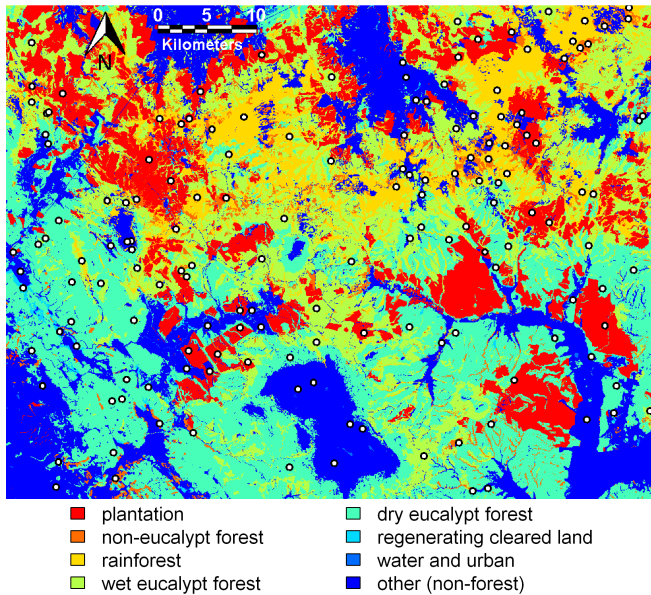


Fig. 3. Overview of broad vegetation communities over the study area (TASVEG map). Circle markers indicate the locations of the training sites selected for the PALSAR forest/non-forest classification (see text for detail).

discussed in [38]. SAR responds to forest structure and dielectric content, while optical sensors rely on a more biochemical response. Discrepancies in radar and optical classifications are therefore incurred due to the way in which radar and optical sensors “see” the land surface and cover.

### 3) Coregistration with PALSAR data

For a proper integration of the thematic information extracted from both datasets, it is crucial for the Landsat and PALSAR data to be accurately coregistered with each other. The registration accuracy between these data was established with the use of a gradient cross-correlation technique [39], which provides a sub-pixel coregistration assessment by detecting and matching features in both images over a window containing many pixels. The displacement between the features in the two images is determined by iteratively searching for the shift (distance and direction) that maximizes the cross-correlation between the data window in each image.

To evaluate the coregistration accuracy between the PALSAR and Landsat data, a total of 299 image features were selected over the study area so as to be uniformly distributed spatially, in both flat and mountainous regions. The average displacement between these features was 0.69 pixel (standard deviation of 0.34 pixel) with 98% of the shifts smaller than 1.5 pixels (at 25m pixel size). Also, the directions of the features’ displacements did not show any apparent signs of systematic coregistration error between the two datasets. Based on these results, the coregistration accuracy between the PALSAR and Landsat images in the region of interest was thus considered satisfactory for the purpose of joint SAR–optical processing.

An assessment of the absolute registration accuracy of the rectified Landsat imagery against independent ground control points (GCPs) was carried out as part of the NCAS program [33]. This analysis demonstrated a Landsat registration

accuracy (best 80% of check GCPs) in the order of 34m (standard deviation of 13.7m) with respect to 1:100,000 topographic maps. As the DEM used in this work is also derived from a state topographic map, and given the lack of systematic spatial displacement between the PALSAR and Landsat data mentioned above, this geolocation accuracy was deemed to provide a sufficient correspondence between the DEM (used in the data pre-processing steps) and each of the SAR and optical data for the purpose of this pilot study.

### D. TASVEG reference data

TASVEG is a Tasmania-wide vegetation map produced by the Tasmanian Vegetation Mapping and Monitoring Program within the Department of Primary Industries and Water ([www.thelist.tas.gov.au](http://www.thelist.tas.gov.au)) [40]. This map comprises 154 distinct vegetation communities mapped at a scale of 1:25,000, and provides a single reference dataset that can be used for a broad range of management and reporting applications relating to vegetation in Tasmania. Aerial photographic interpretation is the primary data collection method for TASVEG, generally at a scale of 1:25,000 and 1:20,000, or 1:42,000 where a better resolution is unavailable. The photo-interpretation is assisted by field verification of representative polygons, and by the use of various vegetation, ecology and geology texts as well as maps containing species information. The resulting line work is then vectorized to form a digital vegetation layer with a positional accuracy of 20m or less, and with a smallest polygon representation of about 0.04ha.

TASVEG is continually revised and updated to reflect changes in the natural environment. The present work draws on the information contained in Version 2.0 of this product, which was released on February 19, 2009. In the region of interest (Ben Lomond bioregion), field work for revision mapping commenced in March 2005 and was completed in October 2008. Over this area, TASVEG shows that most of the land cover belongs to one the following main classes:

- dry eucalypt forest and woodland
- wet eucalypt forest and woodland
- rainforest and related scrub
- non-eucalypt forest and woodland
- plantation (silviculture)
- regenerating cleared land
- urban and water areas
- other (non-forest), such as agriculture and alpine shrubs.

Fig. 3 shows the distribution of these main vegetation communities within the study area. In terms of recentness, spatial resolution and coverage, TASVEG represents the best available ground-truth product for Tasmania at present time. In this work, the TASVEG map (together with other ground and satellite data) is used in the process of selecting training and validation sites for the forest/non-forest classifications.

## III. SAR FOREST CLASSIFICATION

Several methods for F/NF classification using SAR data can be found in the literature (see references in Section I) and could be potentially applied to the data considered here. The

present work adopts the NCAS-LCCP approach to forest classification, which involves the following steps (described in more detail in the following subsections):

1. selection of training sites for the classes of interest
2. use of CVA to derive linear discriminant functions (canonical vectors)
3. selection of separation index and soft classification thresholds using directed contrasts
4. pixel-based classification of the SAR data using the derived index and thresholds.

To the best of the authors' knowledge, this paper represents the first attempt to apply CVA to the problem of F/NF classification of SAR data (see discussion and references in Section I for related classification methods) and demonstrates here that routine processes of the operational NCAS forest mapping system can be readily applied to SAR data.

#### A. Discriminant analysis

CVA is a method to find uncorrelated linear combinations of variables (canonical vectors, CVs) with maximum between-class variability relative to the within-class variability of a set of training data. Consider the case where a total of  $n_i$  ( $i = 1, 2, \dots, C$ ) training sites have been selected for each of  $C$  different classes. In class  $i$ , the  $j$ -th training site is represented by the observation vector  $\mathbf{y}_{ij}$  ( $j = 1, 2, \dots, n_i$ ) which contains the average values of the  $B$  image bands computed over the site's pixels:  $\mathbf{y}_{ij} = (1/p_{ij}) \cdot \sum_{k=1}^{p_{ij}} \mathbf{x}_{ijk}$ , where  $\mathbf{x}_{ijk}$  is a column vector of the  $B$  image bands for pixel  $k$ , and  $p_{ij}$  represents the number of pixels in the  $j$ -th training site of class  $i$ . With  $\mathbf{m}_i = (1/n_i) \cdot \sum_{j=1}^{n_i} \mathbf{y}_{ij}$  representing the mean of the  $i$ -th class, the between-class variation matrix  $\mathbf{B}$  is then defined as

$$\mathbf{B} = \frac{1}{N} \sum_{i=1}^C n_i (\mathbf{m}_i - \bar{\mathbf{m}})(\mathbf{m}_i - \bar{\mathbf{m}})^T \quad (1)$$

$$\bar{\mathbf{m}} = \frac{1}{N} \sum_{i=1}^C n_i \mathbf{m}_i \quad (2)$$

where  $N = n_1 + n_2 + \dots + n_C$ . With  $E\{\cdot\}$  representing the statistical expectation operator, the within-class variation matrix  $\mathbf{W}$  (which is the same for all  $i$  and  $j$ ) is defined as

$$\mathbf{W} = E\{(\mathbf{y}_{ij} - \mathbf{m}_i)(\mathbf{y}_{ij} - \mathbf{m}_i)^T\}. \quad (3)$$

Canonical variate analysis involves finding the vectors  $\mathbf{f}_d$  ( $d = 1, 2, \dots, B$ ) maximizing the ratio  $\mu_d = \mathbf{f}_d^T \mathbf{B} \mathbf{f}_d / \mathbf{f}_d^T \mathbf{W} \mathbf{f}_d$  of between-class to within-class variation; the variable  $\mu_d$  is referred to as the canonical root for vector  $\mathbf{f}_d$ . This approach leads to the following generalized eigenvalue problem:

$$(\mathbf{B} - \mu_d \mathbf{W}) \mathbf{f}_d = 0, \quad \text{for } d = 1, 2, \dots, B, \quad (4)$$

which needs to be solved for  $\mu_d$  and  $\mathbf{f}_d$  subject to

$$\mathbf{f}_i^T \mathbf{W} \mathbf{f}_j = \begin{cases} 1 & \text{if } i = j \\ 0 & \text{otherwise.} \end{cases} \quad (5)$$

The condition in Eq. (5) means that the canonical root  $\mu_d$  represents the magnitude of the between-class variation in the direction  $\mathbf{f}_d$  of maximum between-class variation.

This process can be seen as projecting each class' data onto a line such that the variance of the means of each class on the line is as large as possible relative to the average variance of the observations within each class. Successive projections are defined similarly, subject to being orthogonal (uncorrelated) with previous ones. The canonical roots  $\mu_d$  then provide a measure of separation between classes. The first few canonical vectors  $\mathbf{f}_d$  (with the largest separation) can be used to generate the linear combinations  $s_{dij} = \mathbf{f}_d^T \mathbf{y}_{ij}$  (CV scores), which provide a low-dimensional data reduction for describing class differences. For instance, a plot of the vector  $[s_{1ij}, s_{2ij}]^T$  enables a visual representation of the data known as CV plot. Readers are referred to [36] for further information about the CVA technique.

#### B. SAR classification parameters

In this work, the concepts described in Section III.A are applied with  $C = 2$  classes (forest/non-forest) and  $B = 2$  PALSAR bands (HH and HV). A total of  $N = 160$  training sites were selected across the whole area of interest in such a way as to provide representative samples for each of the broad vegetation communities in the study area; the locations of these training sites are shown as circle markers in Fig. 3. Each site contains roughly 150 to 200 pixels to provide consistency when computing the sites' means. In order to facilitate the attribution to one of the available classes, the sites were selected on the basis of information provided by a combination of aerial photographs, high-resolution imagery (Spot and Ikonos data), the TASVEG data and Landsat imagery.

Based on the selected training sites and the PALSAR data, CVA provided the following two canonical scores:

$$s_{1ij} = 0.076 \cdot HH_{ij} - 1.35 \cdot HV_{ij} \quad (6)$$

$$s_{2ij} = -1.38 \cdot HH_{ij} + 0.43 \cdot HV_{ij} \quad (7)$$

where  $HH_{ij}$  and  $HV_{ij}$  represent the PALSAR data (expressed in dB) averaged over the  $j$ -th training site in the  $i$ -th class. It can be seen that the CV analysis here results in  $s_{1ij}$  being largely defined by the cross-polarization component  $HV_{ij}$ , while  $s_{2ij}$  represents a contrast between the co- and the cross-polarization components. Fig. 4 shows a plot of the vectors  $[s_{1ij}, s_{2ij}]^T$  for all training sites in the resulting CV space. Note that this plot uses colors (and shapes) to represent various subclasses of the two main forest and non-forest groups; this is done for illustration purposes only, and this information (broad

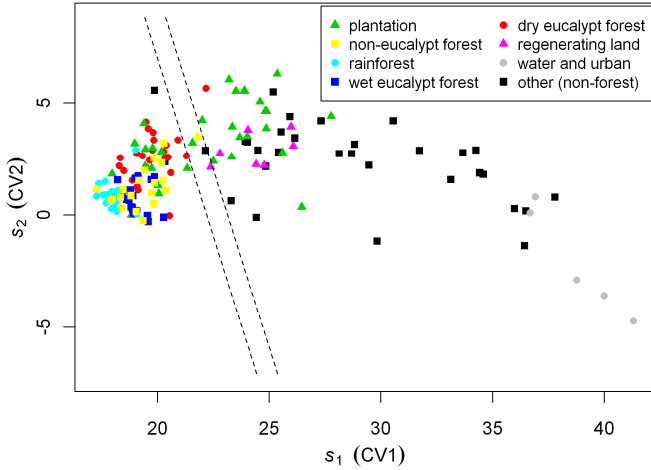


Fig. 4. Plot of training sites' means in CV space (CV plot). The dashed lines indicate the separation between the forest and non-forest classes achieved with the selected classification index and soft thresholds (see text for detail).

vegetation communities) is not actually used in the classification algorithm. This plot shows that most of the forest sites can be clearly separated from the non-forest samples, except for the plantation sites (in green). These sites were selected in areas where forestry activities are taking place, and include samples from both harvested as well as growing/mature plantations, thus explaining the presence of these sites in both the forest and non-forest clusters.

Using the plot in Fig. 4, a spectral index for the forest/non-forest separation is achieved by contrasting two different subsets of training sites (contrast-directed CVA, [41]), where the direction of maximum separation between the two subsets is determined in a manner similar to the derivations in Section III.A. This was achieved here by contrasting all the forest sites against a sub-group of non-forest sites obtained after removing all the clearly separable non-forest sites, namely all sites with  $s_{ij} \geq 27.1$  in Fig. 4. This procedure led to the following separation index, which essentially corresponds to the linear combination of spectral bands allowing the best discrimination between the selected sub-groups of F/NF sites using the available PALSAR data:

$$I = -5.36 \cdot HH + 134.19 \cdot HV. \quad (8)$$

Here, the separation index  $I$  can be interpreted physically as showing that the maximum class separation is achieved by a strong dependence on the HV polarization (two orders of magnitude stronger than the HH coefficient), which is likely to result from volumetric scattering in forest targets. This strong dependence of the SAR F/NF classification on HV (and the limited influence of HH) corroborates the results obtained in previous literature studies (see, e.g., [42]). Further information about the forest discrimination capabilities of the HH and HV channels for different cover types can also be found in [21].

When classifying the PALSAR image, two (soft) thresholds were selected to identify 'certain forest' ( $I_{thr,F}$ ) and 'certain non-forest' ( $I_{thr,NF}$ ) regions in the CV space, allowing the pixels

to be classified as either forest, non-forest or uncertain cover on the basis of their index value. The uncertain cover category contains regions that are not fully separable in the given image, and produce a forest probability value between 0% and 100%. The forest probability  $P_k$  (in %) for a given pixel  $k$  in the SAR image is therefore computed according to the following formula:

$$P_k = \begin{cases} 100 & \text{if } I_k \geq I_{thr,F} \\ 100 \cdot \frac{I_k - I_{thr,NF}}{I_{thr,F} - I_{thr,NF}} & \text{if } I_{thr,NF} < I_k < I_{thr,F} \\ 0 & \text{if } I_k \leq I_{thr,NF} \end{cases} \quad (9)$$

where  $I_k$  is the value of the separation index for pixel  $k$ , as computed according to Eq. (8). Initial values for the soft thresholds were identified by inspection of the CV plot for the training sites (Fig. 4). These thresholds were subsequently fine-tuned manually by visual inspection of the classification results so as to minimize the level of commission error (non-forest pixels assigned to the forest category) and omission error (forest pixels assigned to the non-forest category) over the whole SAR image. This process is similar to that used operationally in the frame of the Landsat-based NCAS monitoring program (see [33] for further detail). In this work, the resulting soft thresholds were set as follows:  $I_{thr,NF} = -2470$  and  $I_{thr,F} = -2370$ . The dashed lines in Fig. 4 show the corresponding discrimination lines (orthogonal to the direction of maximum separation) in CV space.

### C. SAR forest classification

Based on the selected separation index and thresholds, a pixel-based classification is applied to the PALSAR data, with results presented in Fig. 5. The plot on the left shows the resulting SAR forest probability map, which is comparable to the Landsat-based NCAS map (Fig. 2, right). The second image in Fig. 5 shows a comparison of the SAR classification against the TASVEG data. For this purpose, both datasets were collapsed into binary maps of F/NF pixels. For the SAR data, this was achieved by thresholding the forest probability map at the 50% probability level. For TASVEG, pixels from the non-eucalypt forest, rainforest, wet/dry eucalypt forest and plantation classes were grouped into a single forest class, with the remaining pixels labeled as non-forest. The two resulting F/NF datasets are then displayed in a red/green composite image, providing a visual validation of the results that shows the pixels in agreement in black and yellow, and disagreement pixels in red (labeled as forest in TASVEG) and green (labeled as forest in the SAR classification).

This composite image indicates two main sources of disagreement. First, large areas of inconsistency can be seen as red patches across the study area. As seen in Fig. 3, these regions all correspond to plantations, where the TASVEG data is interpreted as being forest regardless of the state of the plantation stands when the SAR imagery was acquired. The SAR data here correctly identifies the red areas in Fig. 5 as

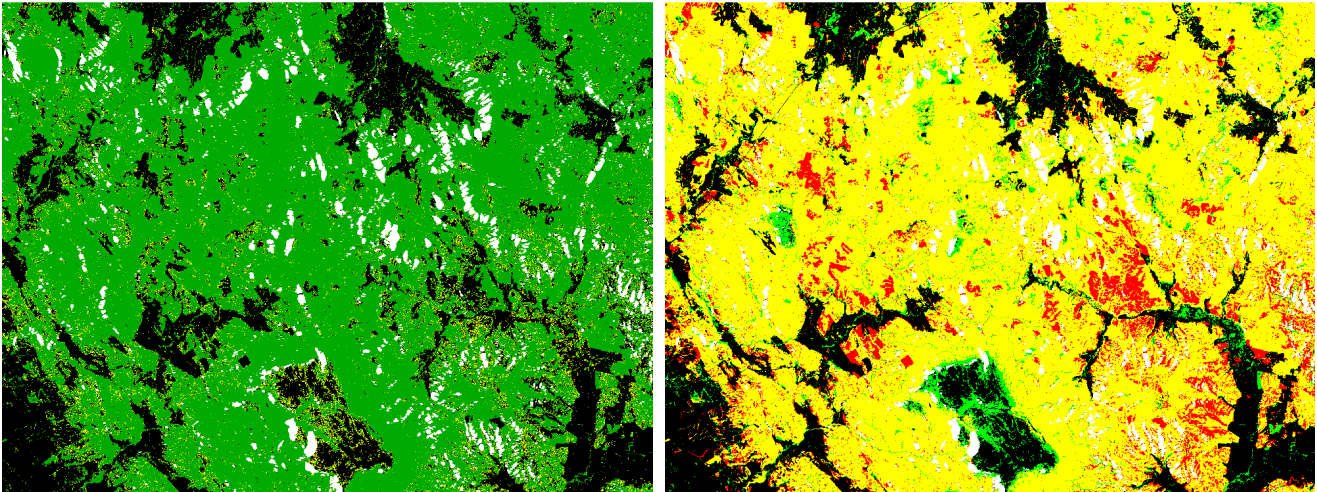


Fig. 5. Single-date SAR forest classification results for 2008. *Left*: classification image of forest probabilities (black: 0%, green: 100%, yellow: other values). *Right*: comparison with TASVEG (red/green composite image), with SAR F/NF results in the green layer and TASVEG F/NF data in the red layer. White areas correspond to the SAR shadow mask. Ben Lomond is the prominent (quasi-rectangular) feature located in the bottom-centre of the images.

TABLE I  
CONFUSION MATRIX BETWEEN TASVEG AND THE SAR CLASSIFICATION  
(SINGLE-DATE F/NF RESULTS).

		TASVEG (%)	
		forest	non-forest
PALSAR (%)	forest	67.57	5.43
	non-forest	8.66	18.34

Values obtained using a total of 5,006,048 pixels (273,952 pixels in shadow areas masked out).

TABLE II  
CONFUSION MATRIX BETWEEN TASVEG AND THE LANDSAT CLASSIFICATION  
(SINGLE-DATE F/NF RESULTS).

		TASVEG (%)	
		forest	non-forest
Landsat (%)	forest	70.16	8.85
	non-forest	7.15	13.84

Values obtained using a total of 5,089,413 pixels (190,587 pixels masked out due to clouds and sensor deficiencies).

being harvested (non-forest), and the corresponding pixels thus cannot be considered as being erroneous.

A second type of discrepancy can be found in higher-altitude rocky plateaus such as the Ben Lomond area (large black and green area in the bottom-centre of the composite image) as well as the Mt. Barrow region (smaller green area in the centre-left of the image). Both areas culminate at an altitude of about 1300m, and the commission errors in the SAR classification result from the presence of alpine/subalpine heath and sedge in these regions (and possibly also due to the influence of surface moisture in these areas of low stature vegetation and bare ground at the time of the SAR acquisition). A CV analysis was performed with additional test sites selected in these areas and showed that these typically cluster together with sites belonging to densely forested regions, thus indicating that this particular type of vegetation (alpine shrubs and bushes) is not fully separable from the forest class using dual-polarization PALSAR data only.

Minor differences between TASVEG and the SAR classification map also appear due to the different mapping resolutions of these two products. For instance, thin features

such as roads and water streams are not always prominent in the SAR imagery and are consequently classified as forest. Other minor differences may also result from the different acquisition times between the datasets (February 2009 revision for TASVEG, September/October 2008 for PALSAR). Outside areas of forestry activities (plantations), the land cover is mostly related to either stable native forests or agricultural land, and such differences can therefore be considered minimal for the study region over the considered time frame.

A further validation of the SAR classification results was established through a pixel-based comparison with TASVEG and indicates an overall agreement of 85.91%. Table I presents the confusion matrix between TASVEG and the SAR F/NF classification, showing the percentages of agreement and disagreement pixels between classes. The differences existing between the SAR-based classification results and other datasets offer an opportunity to further investigate the complementarity of SAR sensors for forest mapping. For completeness, the confusion matrix for the single-date Landsat classification (Fig. 2, right) is also given here in Table II.

Both results can be seen to be similar. The overall agreement between the Landsat classification and TASVEG (84.0%) is here slightly lower than that obtained for the SAR data (85.91%), mainly due to a localized but relatively large area of forest commission error obtained from the optical data in the Ben Lomond region. This difference between the optical and SAR mapping accuracy can here be explained by the fact that the *Tasmania-wide* NCAS forest map is compared to the *locally-trained* (over the study area) SAR classification, which is used in this pilot study for the main purpose of demonstrating the conceptual integration of the PALSAR data within the existing legacy system. Because of the implicit use of different training data, it is important to note that the SAR and optical results presented in Table I and Table II do not necessarily provide appropriate information regarding which sensor is best at extracting forest information over the study area. This kind of determination (i.e., which sensor is best)

does not represent the main focus of the present work, and further research on the specific forest discrimination properties of the PALSAR and Landsat data is reported in [21].

#### IV. JOINT PROCESSING OF SAR AND OPTICAL DATA

In essence, two distinct approaches can be considered for a combination of the available Landsat and PALSAR datasets. One approach is to consider fusion at the data level, where the SAR and optical images are merged into a single dataset which is subsequently used as input to the single-date classification algorithm. This approach, which represents the focus of most of the current literature on SAR–optical data fusion (see, e.g., [5–7], [19], [20]), is not directly applicable in the present study since the PALSAR data is only available for a single epoch (vs. nineteen for Landsat) and is not exactly coincident with the corresponding 2008 Landsat data. This approach can also be problematic in areas where data is missing from one of the considered datasets (e.g., cloud-affected Landsat images).

The second approach consists in considering the alternative data source as an independent addition to the existing time series. The data available at different times (i.e., PALSAR- and Landsat-based single-date forest classifications) can then be assimilated using a multi-temporal methodology, where each forest map is considered as a discrete observation of a continuous process (forest presence/absence) evolving over time. As described in the following, this approach is ideally suited to address issues related to the use of different sensors and non-coincident acquisition times. The multi-temporal approach used in this work was originally presented in [35] and is currently implemented operationally within the Landsat-based NCAS system (see, e.g., [1], [2]). Its use in conjunction with SAR data can be seen as an extension of the NCAS framework to address the issue of multi-sensor integration.

##### A. Multi-temporal processing

Conditional probability networks provide a framework allowing for the assessment and propagation of uncertainty in the classification of multiple data sources of varying quality or accuracy [35]. To improve the forest mapping accuracy, a CPN uses a model which incorporates temporal and spatial rules as well as error rates of the initial classifications.

Let us assume that each image in the time series contains the same number  $K$  of pixels. For the  $k$ -th image pixel ( $k = 1, 2, \dots, K$ ) and  $m$ -th epoch ( $m = 1, 2, \dots, M$ ) in the time series, let  $\mathbf{x}_{km}$  denote the vector of  $B$  image bands, and  $l_{km} \in \{1, 2, \dots, C\}$  denote the corresponding class label estimated by the single-date classifier based on the image data  $\mathbf{x}_{km}$  (and selected training sites). The temporal information for the  $k$ -th image pixel can be gathered by grouping the above variables into sets:  $X_k = \{\mathbf{x}_{k1}, \mathbf{x}_{k2}, \dots, \mathbf{x}_{kM}\}$  and  $L_k = \{l_{k1}, l_{k2}, \dots, l_{kM}\}$ . Also, let  $R_k$  represent the group of eight pixels spatially adjacent to pixel  $k$  (8-pixel neighborhood). Given the multi-temporal data  $X_k$ , the quantities of interest are the “true” class labels  $l'_{km}$  of each pixel in the time series:  $L'_k = \{l'_{k1}, l'_{k2}, \dots, l'_{kM}\}$ .

As applied here, the conditional probability network is a first-order hidden Markov model (HMM) representing the

relationships between the image data and the underlying process of interest. For the  $k$ -th image pixel, this joint spatial-temporal model is defined as follows (see [2], [35]):

$$p(X_k, L_k, L'_k, R_k) = \prod_{m=1}^M Q_1 \cdot Q_2 \cdot Q_3 \cdot Q_4 \quad (10)$$

$$Q_1 = p(\mathbf{x}_{km} | l_{km}) \quad (11)$$

$$Q_2 = p(l_{km} | l'_{km}) \quad (12)$$

$$Q_3 = p(l'_{km} | l'_{(k-1)m}) \quad (13)$$

$$Q_4 = p(l'_{km} | R_k) \quad (14)$$

where for  $Q_3$ ,  $p(l'_{1m} | l'_{0m})$  is simply defined as  $p(l'_{1m})$ .

In this model,  $Q_2$  represents error rates (sensor bias) that weigh the estimated land cover class given the “true” labels, while  $Q_3$  corresponds to temporal rules indicating the likelihood of transition between classes from one epoch to the next. In practice,  $Q_2$  and  $Q_3$  are typically represented as contingency tables that are specified or estimated from the data available. The term  $Q_4$  weighs a pixel’s label towards that of the dominant neighborhood labeling. Following [43],  $Q_4$  is defined as  $p(l'_{km} | R_k) \propto \exp(\alpha + \beta c_k)$ , where  $c_k$  is the number of pixels having the same label as pixel  $k$  in its neighborhood  $R_k$  from the previous iteration of the model;  $\alpha$  and  $\beta$  are user-specified parameters set in this work to 0 and 1, respectively. Assuming a uniform distribution of the class priors  $p(l_{km})$ ,  $Q_1$  corresponds to the likelihood of the estimated class labels given the data at each pixel. This quantity effectively corresponds to the forest probabilities  $P_{km}$  (computed for the  $k$ -th pixel and the  $m$ -th epoch) derived in Eq. (9), i.e.,  $p(\mathbf{x}_{km} | l_{km} = \text{“F”}) = 1 - p(\mathbf{x}_{km} | l_{km} = \text{“NF”}) \propto P_{km}$ .

Applying Bayes’ rule and marginalization to Eq. (10), the probability  $p(L'_k | X_k)$  is computed, providing the maximum likelihood solution for the unobserved “true” class label given the (multi-temporal) data. This is here achieved by using a cyclic ascent algorithm, iteratively cycling over all pixels until convergence on  $L'_k$  is achieved. The details of this algorithm can be found in [34], [35]. The outputs from this spatial-temporal model also represent probability images, one for each time slice, where the forest probabilities have been refined by the temporal rules and error rates defined in the model, so as to provide temporally consistent estimates. Other important properties of the CPN approach can be summarized as follows:

- propagation of uncertainties in the inputs and calculation of uncertainties in the outputs
- production of hard- and soft-decision maps
- handling of missing data by using all available (spatial and temporal) information to make predictions
- existence of well-developed statistical tools for parameter estimation.

This approach provides an efficient probabilistic framework for combining disparate data since variations in data quality

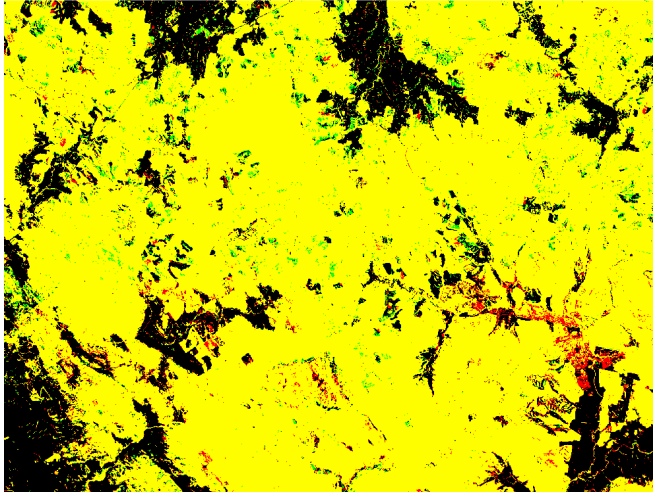


Fig. 6. Comparison of the 2008 classification outputs from the spatial-temporal model (CPN), with combined SAR–optical forest probabilities in the green layer, and all-optical forest probabilities in the red layer (red/green image composite).

and/or missing data can be easily accommodated. As such, this approach thus also provides a useful methodology for the purpose of data fusion of the Landsat and PALSAR datasets considered in this work.

### B. Joint SAR–optical processing

The concept of combined Landsat–PALSAR processing is demonstrated here by means of the following scenario. The NCAS-LCCP time series of Landsat-derived forest probability maps contains a total of nineteen images between 1972 and 2010 (non-uniformly spaced), including one in 2008. These images are used as an input to the CPN, resulting in a first (optical-only) time series of refined forest cover maps. In a second experiment, the Landsat-based forest map for 2008 is removed from the time series and replaced with the forest probability image obtained on the basis of the PALSAR dataset (as described in Section III.C). This leads to a second time series of model outputs, corresponding to refined forest maps obtained from a combination of the SAR and optical datasets into a single product. It must be emphasized here that the model effectively “blends” the data provided in each forest map with the information available from all the preceding and subsequent time slices. In the second scenario, the resulting maps of forest extents for all time steps thus draw on the information contained in both the PALSAR and Landsat data.

The example presented here can be seen as representative of several situations where the complementary nature of SAR can prove advantageous. For instance, the SAR data could be used to fill in potential gaps in the existing optical time series, as in the case of missing data due to clouds, sensor deficiencies, etc. Alternatively, entire maps of SAR-derived forest probabilities could also be added as new time slices so as to improve the temporal resolution of the original time series. ALOS-PALSAR data is available from 2007 and with the anticipated launch of ALOS-2, the continuity of L-band SAR data and contribution to complementary forest monitoring is ensured.

TABLE III  
CONFUSION MATRIX BETWEEN TASVEG AND MULTI-TEMPORAL CLASSIFICATIONS FOR 2008. *TOP*: OPTICAL-ONLY TIME SERIES. *BOTTOM*: COMBINED SAR–OPTICAL TIME SERIES.

		TASVEG (%)	
		forest	non-forest
all-optical (%)	forest	71.51	8.42
	non-forest	5.41	14.66

		TASVEG (%)	
		forest	non-forest
SAR–optical (%)	forest	72.10	7.74
	non-forest	4.82	15.34

### 1) Joint classification results

Fig. 6 presents a comparison of the results for 2008 obtained from the two scenarios considered above. It shows a composite image containing the refined optical-only forest probability map in the red layer, and the combined PALSAR–Landsat forest probability map in the green layer (thresholded at the 50% probability level). A pixel-based comparison of the corresponding F/NF results indicates that these images are 95.8% in agreement. The main differences can be seen to originate from discrepancies between the Landsat and PALSAR single-date forest probability images (see Fig. 2 and Fig. 5). Most of these inconsistencies can be explained by one of the following reasons:

- different thematic information provided by the radar and optical sensors with respect to some ground features
- differences between the Tasmania-wide optimization of the Landsat-based classifier and the locally-optimized SAR classification
- “genuine” differences on the ground between the acquisition dates of the PALSAR and Landsat datasets (as observed in the data itself, e.g., mature plantation harvested and cleared sometime between February and October 2008).

For instance, it can be seen that the Landsat-based single-date forest probability map (Fig. 2, right) erroneously assigns most of the Ben Lomond highland (south of the study area) to the forest class. Because this area is labeled as forest in all the Landsat epochs, the SAR-based non-forest estimates for 2008 appear as spurious in the time series and are consequently re-labeled as forest in the joint classification. Based on this kind of assessment, further research will focus on reducing such discrepancies by improving the Landsat and PALSAR classification, and identifying opportunities for improvements resulting from the complementarity of these two sensors.

As a further validation of the joint classification results, Table III shows the confusion matrices for the all-optical and SAR–optical time series classifications for 2008, as compared to the TASVEG dataset. Here again, both results are very similar with agreement rates of 86.17% (all-optical) and 87.44% (SAR–optical), providing a further demonstration of the interoperable nature of the optical and SAR data for the task of forest mapping and monitoring.

## 2) Summary of forest extents and change

The main task considered in this work is to provide estimates of the forest extents in each epoch as well as changes in forest cover over time (e.g., for carbon accounting purposes). The tables provided in the Appendix present a summary of these parameters computed over the study area for each epoch in the time series. Several observations can be made on the basis of these results:

1. in each epoch (including the 2008 SAR image), the single-date forest maps contain a significant amount of missing data ('null' column in Table IV)
2. the joint spatial-temporal classification predicts labels for the missing data using all other available data, and produces forest maps with non-null probabilities for each pixel in each epoch of the time series (Table V)
3. the joint spatial-temporal classification reduces false transitions between classes (noise).

Furthermore and most importantly, the areas of forest change provided in the 'F→NF' and 'NF→F' columns (conversion between the forest and non-forest classes) in Table V can be seen to be in good agreement between the all-optical and SAR-optical time series at the CPN output. Given the focus of this work on the dynamics of deforestation and re-forestation (land cover change), this result represents a factor of crucial importance for the interoperability of the optical and SAR sensors in forest mapping and monitoring.

## V. CONCLUSION

The work presented in this paper aims to establish a methodology for the classification and the multi-temporal integration of data acquired by different sensors. It provides a realistic and promising demonstration of the integration of multi-temporal ALOS-PALSAR and Landsat imagery for forest mapping and monitoring, and describes the key processing steps involved in a potential approach to this task. In particular, it is shown that the Bayesian concept of a conditional probability network is able to integrate the PALSAR-based forest probability data within a time series of similar Landsat-derived forest maps, producing estimates of forest extents for each time epoch in the presence of missing SAR and optical observations. Within the context of a legacy optical system, this methodology is able to incorporate observations from a newer sensor and produce estimates comparable to those which would otherwise be obtained. Where consistent time-series observations cannot be obtained from a single sensor, this feature may be advantageous for monitoring purposes. This work provides some insight into the interoperability of the SAR and optical sensors, and the framework considered here could thus also incorporate other optical (e.g., SPOT, CBERS, Sentinel 2) and SAR-based (e.g., Radarsat-2, TerraSAR-X, ENVISAT/ASAR) data, although the impacts of sensor biases would need to be considered and will be the topic of future studies. Research work on this project is ongoing and will focus on providing further validation results, as well as extrapolating the findings

presented in this article to larger geographical areas (e.g., to the rest of Tasmania). One aspect of interest when up-scaling the proposed methodology will be to determine whether the use of SAR-specific stratification zones (as done in the Landsat-based system) also has the potential to improve the SAR forest classifications. Future work will also incorporate further PALSAR forest probability maps (from 2007 onwards) and evaluate their influence (bias) on the time-series outputs. The capacity for improved forest extent mapping using multi-frequency SAR data (C- and X-band) will also be investigated.

## APPENDIX

The tables in this appendix provide a summary of forest extents and land cover change over the study region (total area of 330,000ha) for each of the nineteen years in the considered time series, from 1972 to 2010. All values provided in the tables are in hectares (ha).

In the first three columns, Table IV presents the areas of forest (F), non-forest (NF) and missing data (null), computed from the single-date forest classification maps. The other columns summarize the areas of change (transition from one class to another) for each epoch compared to the preceding one. All values are for the Landsat data except for the rows flagged with an asterisk in the first column (year), which are related to the SAR data. The row labeled 2009\* contains the F/NF/null values obtained from the Landsat image (no SAR data available in 2009), but the last nine columns indicate transitions from the SAR-based classes in 2008\* to the Landsat-based classes in 2009. Note that in the considered study area, no data is available for the years 1972 and 1977 (Landsat MSS imagery) due to cloud cover.

Table V contains the forest extents and change values corresponding to the multi-temporal classification results. The left half of the table shows the results for the Landsat-only time series while the right half corresponds to the combined SAR-optical results. These values show how the 'null' pixels in Table IV (and transitions to and from the 'null' class) have been assigned to the forest or non-forest classes following the multi-temporal processing, using information from all available years. Table V also shows that similar hectare counts are obtained for deforestation and re-forestation ('F→NF' and 'NF→F') from the all-optical and the SAR-optical time series, which is of importance for a consistent assessment of land cover change using interoperable SAR and optical sensors.

## ACKNOWLEDGMENT

This project was conducted as part of the GEO-FCT initiative. The authors would like to acknowledge Prof. Tony Milne (Cooperative Research Centre for Spatial Information, Sydney) and Dr. Alex Held (CSIRO AusCover Facility, Canberra) for their help with the acquisition of the PALSAR data, and Dr. Ian Tapley and Prof. Kim Lowell (CRC-SI, Melbourne) for their involvement in this project. We would also like to thank the anonymous reviewers for their helpful comments provided during the preparation of this paper.

TABLE IV

SUMMARY OF FOREST EXTENTS AND CLASS TRANSITIONS OVER THE STUDY AREA: SINGLE-DATE CLASSIFICATIONS. ALL VALUES ARE IN HECTARES (HA).

year	F	NF	null	F→F	F→NF	F→null	NF→F	NF→NF	NF→null	null→F	null→NF	null→null
1972	0.0	0.0	330000.0	0.0	0.0	0.0	0.0	0.0	0.0	0.0	0.0	0.0
1977	0.0	0.0	330000.0	0.0	0.0	0.0	0.0	0.0	0.0	0.0	0.0	330000.0
1980	252926.8	58603.4	18469.8	202288.9	13876.3	36761.6	19417.8	32291.1	6894.5	12193.4	4291.1	18469.8
1985	233900.2	50458.4	45641.4	202288.9	13876.3	36761.6	19417.8	32291.1	6894.5	12193.4	4291.1	18469.8
1988	273173.3	56543.7	283.0	221763.5	12106.3	30.4	12668.0	37693.2	97.3	38741.8	6744.3	155.3
1989	263107.0	65906.4	986.6	255502.3	16885.8	785.2	7591.0	48924.2	28.5	13.7	96.4	172.9
1991	254892.9	54896.1	20211.0	235318.9	8989.9	18798.2	19437.8	45895.7	573.0	136.3	10.5	839.8
1992	255423.5	59763.6	14812.9	228363.8	13926.6	12602.6	8790.6	45239.4	866.0	18269.1	597.6	1344.3
1995	264399.0	65516.5	84.5	242780.9	12641.3	1.3	8296.4	51466.8	0.4	13321.6	1408.4	82.8
1998	264674.9	65221.1	104.0	253308.2	11067.3	23.5	11359.8	54148.6	8.1	7.0	5.1	72.4
2000	260501.6	69483.9	14.5	251697.6	12977.3	0.1	8738.3	56482.8	0.0	65.8	23.8	14.4
2002	240683.3	46251.5	43065.2	222080.4	9876.4	28544.8	18602.8	36374.4	14506.7	0.1	0.7	13.7
2004	57704.7	26744.0	245551.3	50952.5	4927.4	184803.4	2980.0	19975.0	23296.5	3772.2	1841.6	37451.4
2005	246491.8	66193.8	17314.5	54489.4	3208.9	6.4	3216.8	23527.0	0.2	188785.6	39457.8	17307.9
2006	49731.3	26911.8	253357.0	47739.8	3620.5	195131.4	1223.4	23242.8	41727.6	768.0	48.5	16498.0
2007	263054.0	58479.3	8466.8	47697.3	941.8	1092.2	6791.5	19712.2	408.1	208565.2	37825.3	6966.5
2008	250090.9	67997.4	11911.7	235874.7	18917.7	8261.6	6681.4	48354.1	3443.8	7534.8	725.6	206.3
2008*	228312.5	84589.8	17097.8	216721.6	33860.2	12472.2	7553.6	50068.4	857.3	4037.3	661.1	3768.3
2009	229092.4	62401.2	38506.4	214153.2	9653.7	26284.1	9269.4	50997.1	7730.9	5669.9	1750.4	4491.4
2009*	229092.4	62401.2	38506.4	191258.9	12286.4	24767.2	23149.0	49153.6	12287.1	14684.6	961.1	1452.1
2010	249384.5	69846.0	10769.5	210081.3	9474.1	9537.1	12579.9	48794.8	1026.5	26723.3	11577.1	205.9

REFERENCES

[1] P. Caccetta, R. Waterworth, S. Furby, and G. Richards, "Monitoring Australian continental land cover changes using Landsat imagery as a component of assessing the role of vegetation dynamics on terrestrial carbon cycling," in *European Space Agency Living Planet Symposium*, Bergen, Norway, Jun.-Jul. 2010, pp. 1-7.

[2] P. Caccetta, S. Furby, J. O'Connell, J. Wallace, and X. Wu, "Continental monitoring: 34 years of land cover change using Landsat

TABLE V

SUMMARY OF FOREST EXTENTS AND CHANGE FOR THE STUDY AREA: JOINT SPATIAL-TEMPORAL CLASSIFICATION. ALL VALUES ARE IN HECTARES (HA).

year	optical-only time series				SAR-optical time series			
	F	NF	F→F	NF→NF	F	NF	F→F	NF→NF
1972	268663.6	61336.4	-	-	268670.3	61329.8	-	-
1977	268664.4	61335.6	268663.6	0.1	268671.1	61328.9	268670.2	0.1
1980	268664.1	61335.9	268663.4	1.1	268670.4	61329.6	268669.7	1.4
1985	273592.5	56407.5	261715.6	6948.5	273597.9	56402.1	261720.6	6949.9
1988	273175.7	56824.3	270784.2	2808.3	273181.4	56818.6	270789.2	2808.7
1989	271236.2	58763.8	269522.1	3653.6	271241.0	58759.0	269527.6	3653.9
1991	271915.5	58084.5	268652.9	2583.3	271915.0	58085.0	268654.3	2586.7
1992	270603.4	59396.6	269202.0	2713.5	270604.0	59396.0	269201.7	2713.3
1995	270024.1	59975.9	267427.5	3175.9	270018.4	59981.6	267427.4	3176.6
1998	268385.5	61614.5	266263.5	3760.6	268366.2	61633.8	266255.6	3762.9
2000	267904.9	62095.1	266523.6	1861.9	267861.6	62138.4	266501.3	1864.9
2002	270833.6	59166.4	265544.9	2360.1	270820.0	59180.0	265550.8	2310.8
2004	271149.8	58850.3	268772.4	2061.2	271065.9	58934.1	268737.5	2082.5
2005	268688.0	61312.0	266778.4	4371.4	268930.3	61069.8	267060.4	4005.5
2006	269222.9	60777.1	265971.4	2716.6	269641.8	60358.2	266523.1	2407.1
2007	269210.9	60789.1	266536.6	2686.4	269320.6	60679.4	262179.9	2635.9
2008	263729.8	66270.2	262404.6	6806.4	263467.6	66532.4	262179.9	7140.7
2009	261791.9	68208.1	259977.5	3752.3	261583.4	68416.6	258855.4	4612.2
2010	261863.4	68136.6	257704.3	4087.6	261233.8	68766.3	257136.9	4446.5

imagery," in *International Symposium on Remote Sensing of Environment*, San José, Costa Rica, Jun. 2007, pp. 1-4.

[3] C. Brack, G. Richards, and R. Waterworth, "Integrated and comprehensive estimation of greenhouse gas emissions from land systems," *Sustainability Science*, vol. 1, no. 1, pp. 91-106, Oct. 2006.

[4] L. Stowe *et al.*, "Global distribution of cloud cover derived from NOAA/AVHRR operational satellite data," *Advances in Space Research*, vol. 11, no. 3, pp. 51-54, 1991.

[5] Y. Shimabukuro, R. Almeida-Filho, T. Kuplich, and R. de Freitas, "Quantifying optical and SAR image relationships for tropical

- landscape features in the Amazônia," *International Journal of Remote Sensing*, vol. 28, no. 17, pp. 3831–3840, Jan. 2007.
- [6] L. de Carvalho, M. Rahman, G. Hay, and J. Yackel, "Optical and SAR imagery for mapping vegetation gradients in Brazilian savannas: synergy between pixel-based and object-based approaches," in *International Conference on Geographic Object-based Image Analysis*, Ghent, Belgium, Jun.-Jul. 2010, vol. XXXVIII-4/C7, pp. 1–7.
- [7] S. Erasmí and A. Twele, "Regional land cover mapping in the humid tropics using combined optical and SAR satellite data: a case study from Central Sulawesi, Indonesia," *International Journal of Remote Sensing*, vol. 30, no. 10, pp. 2465–2478, Jan. 2009.
- [8] K. Grover, S. Quegan, and C. da Costa Freitas, "Quantitative estimation of tropical forest cover by SAR," *IEEE Transactions on Geoscience and Remote Sensing*, vol. 37, no. 1, pp. 479–490, Jan. 1999.
- [9] E. Podest and S. Saatchi, "Application of multiscale texture in classifying JERS-1 radar data over tropical vegetation," *International Journal of Remote Sensing*, vol. 23, no. 7, pp. 1487–1506, Apr. 2002.
- [10] M. Simard, S. Saatchi, and G. De Grandi, "The use of decision tree and multiscale texture for classification of JERS-1 SAR data over tropical forest," *IEEE Transactions on Geoscience and Remote Sensing*, vol. 38, no. 5, pp. 2310–2321, Sep. 2000.
- [11] R. Almeida-Filho, A. Rosenqvist, Y. Shimabukuro, and J. dos Santos, "Evaluation and perspectives of using multitemporal L-band SAR data to monitor deforestation in the Brazilian Amazônia," *IEEE Geoscience and Remote Sensing Letters*, vol. 2, no. 4, pp. 409–412, Oct. 2005.
- [12] C. Lardeux *et al.*, "Support vector machine for multifrequency SAR polarimetric data classification," *IEEE Transactions on Geoscience and Remote Sensing*, vol. 47, no. 12, pp. 4143–4152, Dec. 2009.
- [13] A. Wijaya and R. Gloaguen, "Fusion of ALOS PALSAR and Landsat ETM data for land cover classification and biomass modeling using nonlinear methods," in *IEEE International Geoscience and Remote Sensing Symposium*, Cape Town, South Africa, Jul. 2009, vol. 3, pp. 581–584.
- [14] M. Sgrenzaroli, A. Baraldi, G. De Grandi, H. Eva, and F. Achard, "A novel approach to the classification of regional-scale radar mosaics for tropical vegetation mapping," *IEEE Transactions on Geoscience and Remote Sensing*, vol. 42, no. 11, pp. 2654–2669, Nov. 2004.
- [15] S. Quegan, T. Le Toan, J. Yu, F. Ribbes, and N. Floury, "Multitemporal ERS SAR analysis applied to forest mapping," *IEEE Transactions on Geoscience and Remote Sensing*, vol. 38, no. 2, pp. 741–753, Mar. 2000.
- [16] D. Hoekman and M. Vissers, "ALOS PALSAR radar observation of tropical peat swamp forest as a monitoring tool for environmental protection and restoration," in *IEEE International Geoscience and Remote Sensing Symposium*, Barcelona, Spain, Jul. 2007, pp. 3710–3714.
- [17] S. Saatchi, J. Soares, and D. Alves, "Mapping deforestation and land use in Amazon rainforest by using SIR-C imagery," *Remote Sensing of Environment*, vol. 59, no. 2, pp. 191–202, Feb. 1997.
- [18] R. Lucas, N. Cronin, A. Lee, M. Moghaddam, C. Witte, and P. Tickle, "Empirical relationships between AIRSAR backscatter and LiDAR-derived forest biomass, Queensland, Australia," *Remote Sensing of Environment*, vol. 100, no. 3, pp. 407–425, Feb. 2006.
- [19] W. Walker, C. Stickler, J. Kellndorfer, K. Kirsch, and D. Nepstad, "Large-area classification and mapping of forest and land cover in the Brazilian Amazon: A comparative analysis of ALOS/PALSAR and Landsat data sources," in *IEEE Journal of Selected Topics in Applied Earth Observations and Remote Sensing*, vol. 3, no. 4, pp. 594–604, Dec. 2010.
- [20] P. Maillard, T. Alencar-Silva, and D. Claudi, "An evaluation of Radarsat-1 and ASTER data for mapping veredas (palm swamps)," *Sensors*, vol. 8, no. 9, pp. 6055–6076, Sep. 2008.
- [21] E. Lehmann *et al.*, "Forest discrimination analysis of combined Landsat and ALOS-PALSAR data," in *International Symposium for Remote Sensing of the Environment*, Sydney, Australia, Apr. 2011, pp. 1–5.
- [22] A. Lopes, R. Touzi, and E. Nezry, "Adaptive speckle filters and scene heterogeneity," *IEEE Transactions on Geoscience and Remote Sensing*, vol. 28, no. 6, pp. 992–1000, Nov. 1990.
- [23] A. Holecz, E. Meier, J. Piesbergen, and D. Nüesch, "Topographic effects on radar cross section," in *CEOS SAR Calibration Workshop*, ESA-ESTEC, Noordwijk, The Netherlands, Sep. 1993, pp. 23–28.
- [24] Sarmap SA, "Synthetic Aperture Radar and SARscape: SAR-Guidebook," September 2008.
- [25] F. Ulaby and M. Dobson, *Handbook of Radar Scattering Statistics for Terrain*. Norwood, MA: Artech House, 1989.
- [26] D. Small, N. Miranda, L. Zuberbühler, A. Schubert, and E. Meier, "Terrain-corrected Gamma: improved thematic land-cover retrieval for SAR with robust radiometric terrain correction," in *European Space Agency Living Planet Symposium*, Bergen, Norway, Jun.-Jul. 2010, pp. 1–8.
- [27] Z.-S. Zhou *et al.*, "Terrain slope correction and precise registration of SAR data for forest mapping and monitoring," in *International Symposium for Remote Sensing of the Environment*, Sydney, Australia, Apr. 2011, pp. 1–4.
- [28] S. Furby, P. Caccetta, X. Wu, and J. Chia, "Continental scale land cover change monitoring in Australia using Landsat imagery," in *International Earth Conference: Studying, Modeling and Sense Making of Planet Earth*, Mytilene, Lesbos, Greece, Jun. 2008, pp. 1–8.
- [29] E. Vermote, D. Tanré, J.-L. Deuzé, M. Herman, and J.-J. Morcrette, "Second simulation of the satellite signal in the solar spectrum, 6S: an overview," *IEEE Transactions on Geoscience and Remote Sensing*, vol. 35, no. 3, pp. 675–686, May 1997.
- [30] X. Wu, T. Danaher, J. Wallace, and N. Campbell, "A BRDF-corrected Landsat 7 mosaic of the Australian continent," in *IEEE International Geoscience and Remote Sensing Symposium*, Sydney, Australia, Jul. 2001, vol. 7, pp. 3274–3276.
- [31] S. Furby and N. Campbell, "Calibrating images from different dates to 'like-value' digital counts," *Remote Sensing of Environment*, vol. 77, no. 2, pp. 186–196, 2001.
- [32] X. Wu, S. Furby, and J. Wallace, "An approach for terrain illumination correction," in *Australasian Remote Sensing and Photogrammetry Conference*, Fremantle, Western Australia, Oct. 2004, pp. 1–9.
- [33] S. Furby, "Land cover change: specification for remote sensing analysis," National Carbon Accounting System, Technical Report no. 9, Australian Greenhouse Office, Canberra, 2002.
- [34] H. Kiiveri, P. Caccetta, N. Campbell, F. Evans, S. Furby, and J. Wallace, "Environmental monitoring using a time series of satellite images and other spatial data sets," in *Nonlinear Estimation and Classification, Lecture Notes in Statistics*, vol. 171, D. Denison, M. Hansen, C. Holmes, B. Mallick, and B. Yu, Eds. New York: Springer-Verlag, 2003, pp. 49–62.
- [35] P. Caccetta, "Remote sensing, geographic information systems (GIS) and Bayesian knowledge-based methods for monitoring land condition," Ph.D. thesis, Curtin University of Technology, School of Computing, 1997.
- [36] N. Campbell, "Canonical variate analysis – A general model formulation," *Australian and New Zealand Journal of Statistics*, vol. 26, no. 1, pp. 86–96, Apr. 1994.
- [37] J. O'Connell and P. Caccetta, "Testing of alternate classification procedures within an operational, satellite based, forest monitoring system," in *Innovations in Remote Sensing and Photogrammetry, Lecture Notes in Geoinformation and Cartography*, vol. 2, S. Jones and K. Reinke, Eds. Berlin Heidelberg: Springer-Verlag, 2009, pp. 121–132.
- [38] S. Furby and X. Wu, "Evaluation of alternative sensors for a Landsat-based monitoring program," in *Innovations in Remote Sensing and Photogrammetry, Lecture Notes in Geoinformation and Cartography*, vol. 2, S. Jones and K. Reinke, Eds. Berlin Heidelberg: Springer-Verlag, 2009, pp. 75–90.
- [39] N. Campbell and X. Wu, "Gradient cross correlation for sub-pixel matching," in *Congress of the International Society for Photogrammetry and Remote Sensing*, Beijing, China, Jul. 2008, vol. 7, pp. 1065–1070.
- [40] "Tasmanian Vegetation Monitoring and Mapping Program: TASVEG 2.0 Metadata (Feb. 2009 release)," Tasmanian Vegetation Monitoring and Mapping Program, Resource Management and Conservation Division, Department of Primary Industries and Water, Feb. 2009.
- [41] N. Campbell and S. Furby, "Variable selection along canonical vectors," *Australian and New Zealand Journal of Statistics*, vol. 36, no. 2, pp. 177–183, Jun. 1994.
- [42] E. Mitchard *et al.*, "Using satellite radar backscatter to predict above-ground woody biomass: A consistent relationship across four different African landscapes," *Geophysical Research Letters*, vol. 36, Dec. 2009.
- [43] J. Besag, "On the statistical analysis of dirty pictures," *Journal of the Royal Statistical Society*, vol. 48, no. 3, pp. 259–302, 1986.